Zhen Lei
Hongming Lyu ✉

https://doi.org/10.21278/TOF.501073724
ISSN 1333-1124
eISSN 1849-1391

REGENERATIVE BRAKING CONTROL OF ELECTRIC VEHICLES USING ELECTRO-MECHANICAL BRAKES BASED ON IMPROVED WHALE OPTIMISATION ALGORITHM

Summary

To improve the energy utilisation efficiency and driving range of electric vehicles, this paper proposes two strategies: a brake energy recovery control strategy and an electric braking force optimisation algorithm based on electro-mechanical brakes (EMBs). First, a three-stage control system for the EMBs is designed using an active disturbance rejection control (ADRC) algorithm. Next, a brake force distribution strategy that uses a safety zone rule to dynamically adjust the brake force distribution according to real-time operating conditions is proposed based on the ideal brake force distribution curve and the ECE regulation line. This ensures effective braking performance. Then, the whale optimisation algorithm (WOA) is introduced with improvements to its adaptive inertia weight and nonlinear convergence factor to optimise the motor torque control and improve the braking energy recovery efficiency. Finally, co-simulations were performed in MATLAB/Simulink and AVL Cruise for two typical conditions: the worldwide harmonised light vehicle test cycle (WLTC) and China light-duty vehicle test cycle (CLTC). The simulation results show that the three-stage control system designed with the ADRC algorithm outperforms the standard EHB system and that the optimised motor braking force using the improved WOA can recover more energy during braking.

Key words: *electro-mechanical braking system; active disturbance rejection control; improved whale optimisation algorithm; braking energy recovery*

1. Introduction

In recent years, the continuous rise in global automobile ownership has improved daily life significantly, but it has also led to social challenges, such as energy shortages, environmental pollution, and traffic congestion [1]. Due to their zero emissions, simplified design, and capacity for regenerative braking, which enhances overall energy efficiency and extends driving range, electric vehicles (EVs) have gained considerable attention [2]. In line with trends in automotive electrification, intelligence, and connectivity, braking systems are increasingly required to integrate features such as brake-by-wire technology. Compared to traditional hydraulic brakes, electro-mechanical brakes (EMBs) offer advantages such as a compact structure, rapid response time, and seamless integration with vehicle dynamics control (VDC) systems. These features are essential for advanced intelligent driving, bringing EMBs into the focus of automotive manufacturers.

The EMB control system's key feature is its ability to accurately apply braking force to the disc, achieving precise and rapid control. Park et al. [6] used an angle sensor to measure the motor angle and estimate the clamping force based on its functional relationship. Fu et al. [7] monitored the displacement of the ball screw to estimate the clamping force. Ki et al. [8] implemented a pressure-speed loop and a position-speed loop to switch the control according to braking conditions. Li et al. [9] introduced a novel clamping force model that utilises linear transformations of two polynomial functions. They also proposed a unified architecture that ensures a smooth transition between the gap closure and the clamping force tracking. Line et al. [10] addressed actuator saturation, load-dependent friction, and nonlinear stiffness in EMBs using gain scheduling, friction compensation, and feedback linearisation techniques. Incorporating a model predictive controller allows the system's motor torque to be utilised more effectively to achieve precise control. Wei et al. [11] applied the direct torque control technology to the permanent magnet synchronous motor (PMSM) in the EMB system to improve the clamping force control in the actuator. Lee et al. [12] developed a clamping force compensation algorithm that uses powerful actuators of the EMBs, rigid transmission, and high-bandwidth tracking to actively manage brake torque variations and mitigate brake chatter caused by geometric defects on the brake disc surface. This study eliminates reliance on traditional clamping force sensors, thereby reducing the risk of sensor failure due to high brake disc temperatures.

The most prominent issue currently facing electric vehicles is driving range. There are two primary strategies to enhance the range: developing batteries with higher energy density, which often requires extensive research and development and considerable costs, or implementing energy recovery technologies in electric vehicles. The latter has seen notable advancements and applications [13, 14]. Che et al. proposed a regenerative braking power calculation method and a control strategy based on a genetic algorithm to address regenerative braking energy recovery issues [15]. Li et al. [16] introduced a regenerative braking control strategy that estimates road slope angles to mitigate significant energy loss in downhill scenarios. Zheng et al. [17] and Zhang et al. [18] proposed an electro-mechanical composite braking control strategy that uses a fuzzy algorithm to optimise the electric vehicle's power and enhance its driving range. Mei et al. proposed a new fuzzy sliding mode control scheme based on an adaptive control strategy to maximise battery energy recovery [19]. Currently, most regenerative braking technology research focuses on vehicles with electronic hydraulic brakes (EHBs), while studies on vehicles with EMBs are limited.

Addressing this issue, this paper proposes a regenerative braking control strategy utilising an EMB system in electric vehicles. It designs a clamping force control strategy based on active disturbance rejection control (ADRC), complemented by a three-stage closed-loop control strategy that enhances the EMB's response speed and tracking accuracy. The paper also proposes a safety domain-based brake force distribution scheme for the front and rear axles and employs an improved whale optimisation algorithm (WOA) to optimise the motor braking force.

The structure of this paper is as follows: Section 1 introduces the structure and principle of the EMB system. Section 2 elaborates on the design of the three-stage control strategy based on ADRC for the EMB system. Section 3 presents the brake force distribution scheme for the front and rear axles of electric vehicles. Section 4 outlines the basic principles of the WOA and its enhancements and explains how it is applied to optimise the motor braking force. Section 5 provides a co-simulation analysis to validate the proposed control strategy. Finally, Section 6 concludes the paper.

2. Modelling of the EMB system

2.1 Structure and working principle of the EMB system

Unlike traditional hydraulic braking systems, the EMB system uses a mechatronic design that replaces the conventional hydraulic power structure with a torque motor to brake the vehicle. The EMB system consists of an onboard power supply, a brake pedal unit, a central

control unit, an onboard computer network, a control unit, and an actuator. The actuator includes a drive motor, planetary gear, and ball screw, which facilitate mechanical braking [20]. The structure of the EMB actuator (disc type) is illustrated in Fig. 1.

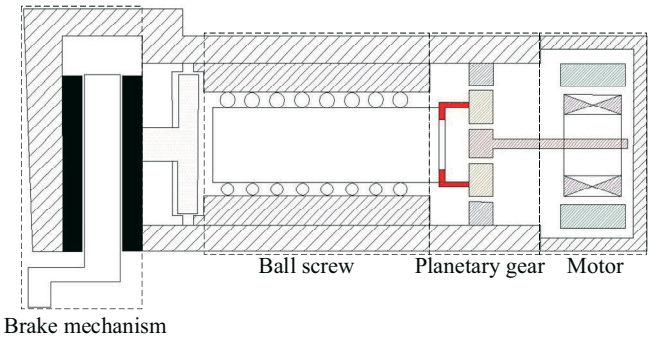

Fig. 1 Structure of the EMB actuator (disc type)

When the driver initiates braking based on external conditions and vehicle information, he or she depresses the brake pedal. This action activates a sensor that detects the pedal travel and sends a signal to the central control unit. The central control unit then processes this input to calculate the optimal clamping force for each wheel in real time, communicating this information to the actuator control unit. Upon receiving the braking signal, the EMB actuator adjusts the motor's rotation via the planetary gear to facilitate deceleration and increase torque. The rotary motion is then converted to linear motion via the ball screw, which pushes the brake pad against the brake disc to achieve effective braking.

2.2 Electromagnetic properties

A PMSM is selected as the driving motor of the EMB system, which is a nonlinear system. After the coordinate transformation, the voltage equation is given by [21]

$$\begin{bmatrix} u_a \\ u_b \\ u_c \end{bmatrix} = \begin{bmatrix} R_s & 0 & 0 \\ 0 & R_s & 0 \\ 0 & 0 & R_s \end{bmatrix} \begin{bmatrix} i_a \\ i_b \\ i_c \end{bmatrix} + \frac{\mathrm{d}}{\mathrm{d}t} \begin{bmatrix} \psi_a \\ \psi_b \\ \psi_c \end{bmatrix}. \tag{1}$$

The flux linkage equation is given by

$$\begin{bmatrix} \psi_a \\ \psi_b \\ \psi_c \end{bmatrix} = \begin{bmatrix} L_{aa} & M_{ab} & M_{ac} \\ M_{ba} & L_{bb} & M_{bc} \\ M_{ca} & M_{cb} & L_{cc} \end{bmatrix} \begin{bmatrix} i_a \\ i_b \\ i_c \end{bmatrix} + \psi_f \begin{bmatrix} \cos(\theta) \\ \cos(\theta - 2\pi/3) \\ \cos(\theta + 2\pi/3) \end{bmatrix}, \tag{2}$$

where u_a, u_b, u_c are the voltages of each phase of the motor, i_a, i_b, i_c are the currents of each phase of the motor, R_s is the resistance of the motor, L_{aa}, L_{bb}, L_{cc} are the self-inductances of each phase winding of the stator, M_{ab}, M_{ba}, Mac, M_{ca}, M_{bc}, M_{cb} are the mutual inductances between each phase winding of the stator, and ψ_a, ψ_b, ψ_c are the three-phase stator fluxes of the motor. ψ_f is the permanent magnet flux of the motor rotor.

2.3 Frictional behaviour

The Stribeck model is adopted to describe the friction damping behaviour of the drive motor. Its mathematical expression is defined as follows [22]:

$$T_f = \begin{cases} T_f(\omega) & \omega \neq 0 \\ T_e & \omega = 0,\ |T_e| < T_s \\ T_s \operatorname{sgn}(T_e) & \omega = 0,\ |T_e| \geq T_s \end{cases}, \tag{3}$$

where $T_f(\omega)$ is the function describing the Stribeck phenomenon, T_s is the maximum static friction torque, T_e is the system static friction torque, and ω is the motor speed.

The Gauss model is used as the function to describe the Stribeck effect. The mathematical expression takes the following form:

$$T_f(\omega) = \left(T_c + \left(T_s - T_c\right)e^{-(\omega/\omega_s)^{\sigma_1}}\right)\mathrm{sgn}(\omega) + \sigma\omega\,. \tag{4}$$

2.4 Load torque

The torque output of the drive motor is transmitted through the mechanical linkage and ultimately converted into clamping force on both sides of the brake disc. Concurrently, this generated clamping force exerts a reaction on the drive motor, resulting in load torque. The mathematical expression of this relationship is as follows:

$$F_n = \begin{cases} A_1\Delta s^3 + A_2\Delta s^2 - A_3\Delta s + A_4 & s > 0.18 \\ B\Delta s & 0 < s \le 0.18 \\ 0 & s < 0 \end{cases}. \tag{5}$$

Then, the load torque of the clamping force acting on the motor is given by

$$T_l = \frac{F_n \cdot L}{2 \cdot \pi \cdot i_p \cdot \eta_g \cdot \eta_s}, \tag{6}$$

where F_n is the clamping force, Δs is the difference between the screw nut displacement s and the brake clearance s_w, T_l is the load torque, L is the lead of the ball screw, η_s is the transmission efficiency of the ball screw, η_p is the transmission efficiency of the planetary gear, and i_p is the reduction ratio of the planetary gear.

2.5 Transmission mechanism

The EMB transmission mechanism consists of a planetary gear and a ball screw. Its transmission ratio is expressed as

$$s = \frac{\theta \cdot L}{2 \cdot \pi \cdot i_p}, \tag{7}$$

where θ is the motor angle.

3. EMB control strategy

The EMB system executes the entire braking process in three stages: brake gap elimination, clamping force tracking, and brake gap regeneration [23]. Consequently, a closed-loop control is implemented for each stage, with a focus on stage two, where an ADRC strategy is designed to improve the clamping force tracking accuracy.

3.1 Brake gap elimination

Control of the drive motor is critical to the EMB system, because it requires a rapid response to the system inputs. During this stage, the motor primarily works to overcome its own frictional resistance. To efficiently eliminate the brake gap, the target speed is set to the maximum speed of the motor, using a speed-current dual-loop control approach.

3.2 Clamping force tracking

Once the brake gap is eliminated, the brake pads engage the brake disc to generate clamping force. The effectiveness of the control system at this stage influences not only the

stopping distance and stability of the vehicle but also passenger comfort. To enhance the clamping force tracking accuracy and minimise the system overshoot, a three-loop closed-loop control system involving clamping force, speed, and current is designed, as illustrated in Fig. 2.

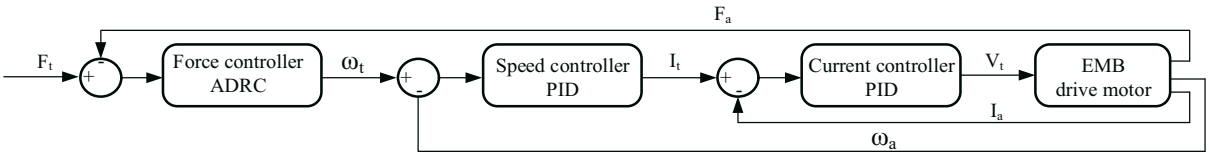

Fig. 2 EMB system control flowchart

The ADRC method consolidates all the uncertain factors affecting the controlled object into unknown disturbances. Using input and output data from the controlled object, it estimates and compensates for these disturbances [24]. The control system consists primarily of a tracking differentiator (TD), an extended state observer (ESO), and nonlinear state error feedback (NLSEF). The EMB system is treated as a second-order nonlinear system for which an active disturbance rejection controller is developed.

The equation of state for the second-order system is given by

$$\begin{cases} \dot{x}_1 = x_2 \\ \dot{x}_2 = f(x_1, x_2, w(t)) + b \cdot u(t) \\ y = x_1 \end{cases}, \tag{8}$$

where $u(t)$ and y are the input and the output, respectively, $\dot{x}_1$ and $\dot{x}_2$ are system state variables, f is the total disturbance synthesised inside and outside the system, and b is the gain.

The TD enables a smooth transition of the input signal from its initial value to its target value, and the duration of this process is adjustable. Both the transition process and the differentiator are implemented in a single module. Its discrete algorithm is given by

$$\begin{cases} f(h) = \text{fhan}(x_1(k) - v(k), x_2(k), r, h_0) \\ x_1(k+1) = x_1(k) + hx_2k \\ x_2(k+1) = x_2(k) + hfh \end{cases}, \tag{9}$$

where x_1 is the tracking signal of the input signal, x_2 is the differential signal of the input signal, h is the sampling period, $v(k)$ is the target signal of the input, and fhan is a fastest synthetic function, defined as follows:

$$\begin{cases} d = rh_0^2 \\ a_0 = h_0 x_2 \\ a_1 = \sqrt{d(d + 8|y|)} \\ a_2 = a_0 + \text{sgn}(y)(a_1 - d)/2 \\ y = x_1 + a_0 \\ s_y = \dfrac{(\text{sgn}(y+d) - \text{sgn}(y-d))}{2} \end{cases} \tag{10}$$

$$\begin{cases} a = (a_0 + y - a_2)s_y + a_2 \\ s_a = \dfrac{(\text{sgn}(a+d) - \text{sgn}(a-d))}{2} \\ \text{fhan} = -r(a/d - \text{sgn}(a))s_a - r\,\text{sgn}(a) \end{cases}, \tag{11}$$

where r is the speed factor and h_0 is the filter factor.

The ESO reformulates the total disturbance of the system as a new state variable. This variable is estimated and compensated for using the system's inputs, outputs, and applied control inputs. Its mathematical expression is given by

$$\begin{cases} e(k) = z_1(k) - y(k) \\ z_1(k+1) = h\left(z_2(k) - \beta_{01} e(k)\right) + z_1(k) \\ z_2(k+1) = h\begin{pmatrix} z_3(k) + b_0 u \\ + f_0(z_1, z_2) \end{pmatrix} + z_2(k) \\ z_3(k+1) = h + z_3(k) \end{cases} \tag{12}$$

$$\mathrm{fal}(e, \alpha, \delta) = \begin{cases} \dfrac{e}{\delta^{1-\alpha}} \\ |e|^{\alpha} \operatorname{sgn}(e) \end{cases}, \tag{13}$$

where $z_1(t)$ and $z_2(t)$ are the estimated values of the system state variables $x_1(t)$ and $x_2(t)$, respectively, and $z_3(t)$ represents the observed values of the expanded disturbed state variables. The parameters β_{01}, β_{02}, β_{03} and δ are the control parameters, while α is the control parameter of the function fal.

The NLSEF control is particularly effective for systems with unknown exact models. The error between the tracking signal x_1 and the differential signal x_2 generated by the tracking differentiator, along with the corresponding state variable estimates z_1 and z_2, produced by the extended state observer, serves as input to the nonlinear feedback controller. This configuration results in a closed-loop control system. The algorithm is outlined as follows:

$$\begin{cases} e_1 = x_1 - z_1 \\ e_2 = x_2 - z_2 \\ u_0 = k(e_1, e_2, p) \end{cases} \tag{14}$$

$$\begin{gathered} u_0 = \beta_1 \mathrm{fal}(e_1, a_1, \delta) + \beta_2 \mathrm{fal}(e_2, a_2, \delta) \\ 0 < a_1 < 1 < a_2 \end{gathered}, \tag{15}$$

where u_0 is the error feedback control quantity, k is the error feedback rate, and β_1 and β_2 are the control parameters.

The output of the ADRC in the clamping force loop represents the target value for the q-axis current of the PMSM. Therefore, the expression for the clamping force control is as follows:

$$i_q = \frac{u_0 - z_3(t)}{b_0} = \frac{\beta_1 fal(e_1, a_1, \delta) + \beta_2 fal(e_2, a_2, \delta)}{b_0}. \tag{16}$$

3.3 Brake gap regeneration

Following the clamping force tracking stage, the target clamping force is set to zero. Due to the internal friction within the system and the absence of a self-adjusting mechanism in the EMB system, it is necessary to reverse the motor to separate the brake pad from the brake disc, thereby creating a fixed brake gap. This stage employs a position-speed-current three-loop closed-loop control system.

4. Regenerative braking control strategy for EVs

4.1 EMB-based regenerative braking system

The braking system of a front-wheel drive electric vehicle consists primarily of three subsystems: an EMB system, a motor brake system, and a brake control system [25]. Fig. 3 shows the structure of the EMB-based regenerative braking system.

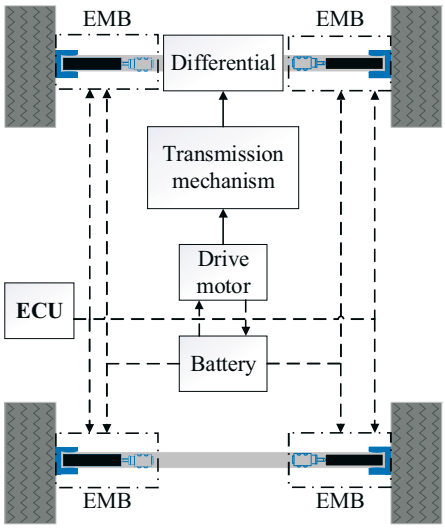

Fig. 2 EMB-based vehicle regenerative braking system

This composite braking system effectively distributes the braking force between the front and rear axles, resulting in safer and more stable braking performance at varying intensities. Optimising the distribution of braking forces enhances the efficiency of regenerative braking. Improving the performance of the electric motor also enhances regenerative braking capabilities [26].

During braking, the regenerative braking controller receives real-time vehicle information and calculates the front axle braking force F_f and the rear axle braking force F_r. The front axle braking force F_f is then sent to the improved WOA, which yields the optimised front axle EMB braking force F_{f_EMB} and the electrical braking force F_{f_re} [27]. The overall structure is depicted in Fig. 4.

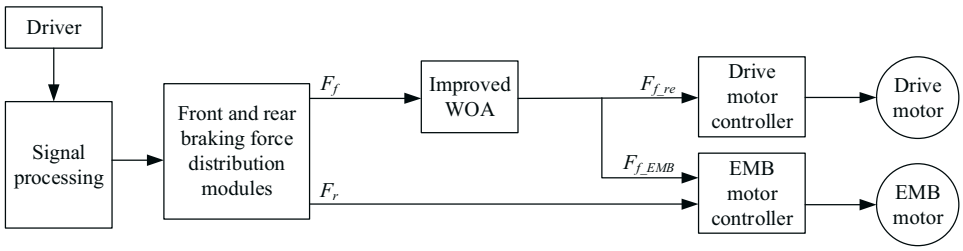

Fig. 4 Control flowchart of regenerative braking system

4.2 Braking force distribution strategy for front and rear axles

The braking force distribution curve for the front and rear axles should remain above the ECE regulation line while staying below the ideal *I*-curve. The designed braking force distribution curves for the front and rear axles are represented by the red line in Fig. 5. Given that the focus is on a front-wheel-drive electric vehicle, the braking force should be distributed preferentially to the front axle to maximise energy recovery. However, this distribution must be controlled to the left of the *f*-line to prevent front wheel lockup and ensure directional stability during braking.

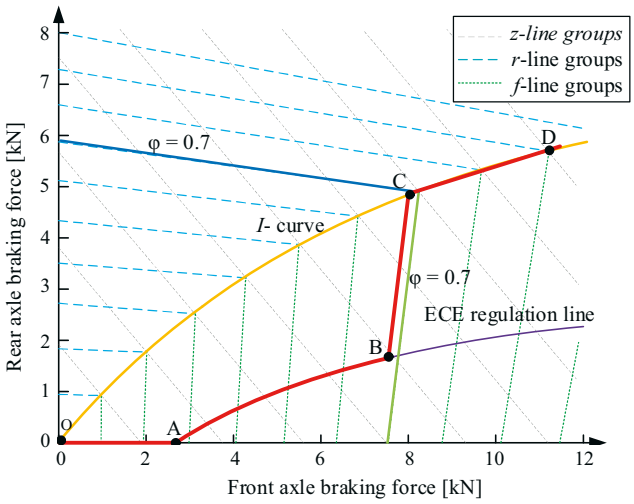

Fig. 5 Braking force distribution curve

Low-intensity braking (0<z<0.22): This corresponds to the OA segment in the figure, in which only the front axle motor engages in braking while the rear wheel EMB remains inactive.

Medium-intensity braking (0.22<z<0.49): Represented by the AB segment, both the EMB system and the front axle motor participate in braking simultaneously.

High-intensity braking (0.49<z<0.68): Corresponding to the BC segment, both the EMB system and the front axle motor engage in braking, with the EMB system exerting a greater braking force.

Emergency braking (z>0.68): This is illustrated by the CD segment, where regenerative braking from the front axle motor stops, and the EMB provides the braking force for both axles.

5. Regenerative braking control strategy for EVs

The motor plays a crucial role in energy recovery during braking. Based on the designed braking force distribution for the front and rear axles, the regenerative power of the motor is optimised to enhance energy recovery efficiency. An improved WOA is employed to optimise the ratio of the motor braking force to the EMB braking force on the front axle.

In the context of the problem of braking force distribution addressed in this paper, the objective function—aimed at maximising energy recovery efficiency while satisfying braking stability constraints—is a typical non-convex problem with multiple local optima. Traditional methods such as gradient descent are prone to getting trapped in local optima and often fail to locate the global or near-global optimal solution. Compared to other heuristic algorithms, such as genetic algorithm (GA) and particle swarm optimisation (PSO), the WOA demonstrates advantages such as the existence of fewer parameters, a simpler structure, and a better balance between exploration and exploitation capabilities.

5.1 WOA principle

The WOA is a novel heuristic optimisation technique that mimics the hunting behaviour of humpback whales. In the WOA, each whale's position represents a feasible solution. Humpback whales utilize a unique hunting strategy called the bubble-net attack, as shown in Fig. 6 [28].

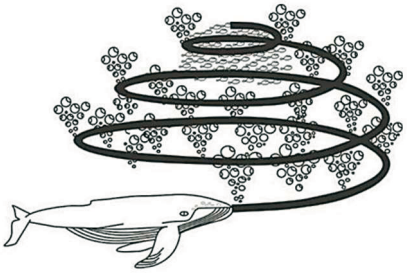

Fig. 6 Bubble-net feeding behaviour of humpback whales

When whales detect small fish and shrimps, they spiral beneath and surround their prey with exhaled bubbles, swimming in a circular or "9" shape to maximise their ability to encircle the prey and gradually bring it closer until it can be consumed.

During this feeding process, the whales collaborate to locate the prey. Once one whale locates the prey, the others converge to participate in the feeding. In the context of the WOA, each whale represents a solution, while the group represents multiple solutions. Throughout the optimisation process, the whales continuously update their positions until a satisfactory solution is achieved [29].

5.2 Whale optimisation algorithm (WOA)

The process of WOA consists of the following three main steps.

5.2.1 Encircling prey

In the hunting process, whales first locate their prey and then encircle it. In the WOA, the optimal solution corresponds to the position of the lead whale, which acts as the prey. Once the optimal whale position is identified, the other whales update their positions by moving toward it. Initially, the distance between each whale and the optimal whale position needs to be calculated, thus

$$\boldsymbol{D}=|C\boldsymbol{X}^{*}(t)-\boldsymbol{X}(t)| \tag{17}$$

$$\boldsymbol{X}(t+1)=\boldsymbol{X}^{*}(t)-A\boldsymbol{D}, \tag{18}$$

where t represents the current iteration, $\boldsymbol{X}^{*}(t)$ denotes the position vector of the best solution obtained so far, $\boldsymbol{X}(t)$ is the position vector at iteration t, $\boldsymbol{D}$ is the distance between the current individual whale and the current optimal solution, and A and C are two coefficients which can be calculated as follows:

$$A=2ar-a \tag{19}$$

$$C=2r, \tag{20}$$

where r is a random number in [0,1], and a is a convergence factor that linearly and iterative decreases from 2 to 0 over the course of iterations (in both exploration and exploitation phases).

$$a=2-2t/t_{\max,} \tag{21}$$

where $t_{\max}$ is the maximum number of iterations.

5.2.2 Bubble-net attacking method (exploitation phase)

The bubble-net method employed by humpback whales is unique among marine creatures. This method can be mathematically formulated in two stages: the shrinking encircling mechanism and the spiral updating position.

a) Shrinking encircling mechanism

This stage involves a parameter A that decreases in range from $-a$ to a, with the value of a decreasing linearly, as shown in Eq. (19). If A is constrained to the range [−1, 1], the current position $\boldsymbol{X}(t)$ of a search agent will be updated to lie between $\boldsymbol{X}(t)$ and the best agent's position $\boldsymbol{X}^*(t)$.

b) Spiral updating position

The distance between the current position of a search agent and the best position is calculated, and a spiral is generated using the spiral equation that connects these positions.

$$\boldsymbol{X}(t+1)=\boldsymbol{X}^*(t)+\boldsymbol{D}_p e^{bl}\cos(2\pi l), \tag{22}$$

where $\boldsymbol{D}_p=|\boldsymbol{X}^*(t)-\boldsymbol{X}(t)|$ is the distance between the current search agent and the best one, b denotes a constant variable used to define the logarithmic spiral's shape, and l is a randomly generated value in the range [−1, 1].

These whales move around the prey or the best positions in a shrinking spiral-shaped path, choosing between shrinking circles or spiral trajectories based on a 50% probability. This movement and probability are mathematically formulated as follows:

$$\boldsymbol{X}(t+1)=\begin{cases}\boldsymbol{X}^*(t)-A\boldsymbol{D} & p<0.5\\ \boldsymbol{X}^*(t)+\boldsymbol{D}_p e^{bl}\cos(2\pi l) & p\geqslant 0.5\end{cases}, \tag{23}$$

where p is a random value in range [0,1].

5.2.3 Search for prey (exploration phase)

Another searching behaviour in the WOA is exploration, which utilises the values of A. As previously mentioned, the exploitation phase occurs when the value of A is between −1 and 1. Conversely, the exploration phase is executed when A is less than −1 or greater than 1, meaning that it falls outside the range [−1, 1]. During this phase, the current search agent moves away from the best search agent and updates its position based on a randomly chosen selected agent. This phase is mathematically formulated as follows:

$$\boldsymbol{D}=|C\boldsymbol{X}_{\text{rand}}(t)-\boldsymbol{X}(t)| \tag{24}$$

$$\boldsymbol{X}(t+1)=\boldsymbol{X}_{\text{rand}}(t)-A\boldsymbol{D}, \tag{25}$$

where $\boldsymbol{X}_{\text{rand}}$ is a random position vector (a random whale) chosen from the current population.

5.3 Improved WOA

5.3.1 Adaptive inertia weight

In the WOA, the inertia weight w is introduced to enhance the algorithm's convergence to the global optimal solution. A larger inertia weight improves the algorithm's global optimisation capability, while a smaller inertia weight enhances its local optimisation ability, thus boosting the overall performance of the algorithm. Therefore, this section proposes the use of inertia weight to improve the algorithm. The expression for the inertia weight is as follows:

$$w=\frac{1}{2}\sin\left(\frac{\pi t}{T_{\max}}+\frac{\pi}{2}\right)-\frac{1}{2}. \tag{26}$$

Then, the updated formula for the position vector update takes the following form:

$$\boldsymbol{X}(t+1)=w\boldsymbol{X}^*(t)-A\boldsymbol{D} \qquad p<0.5 \tag{27}$$

$$\boldsymbol{X}(t+1)=w\boldsymbol{X}^*(t)+\boldsymbol{D}_p e^{bl}\cos(2\pi l) \quad p>0.5. \tag{28}$$

The inertia weight *w* decreases nonlinearly as the number of iterations increases, making the algorithm suitable for global optimisation in the early stages and local optimisation in the later stages. This approach enhances both the convergence accuracy and the convergence speed.

Unlike common linear or cosine-based inertia weight strategies that decrease monotonically, our proposed adaptive inertia weight strategy is non-monotonic and directly linked to population distribution diversity. Specifically, the inertia weight adjusts dynamically based on the concentration of individuals within the current population. This concentration is measured by calculating the average distance between individuals. When the population diversity is high, the inertia weight increases to enhance global exploration. When the population tends to converge, the inertia weight decreases to strengthen local exploitation. This dynamic feedback mechanism allows for a smarter balance of exploration and exploitation than fixed variation patterns.

5.3.2 Nonlinear convergence factor

The WOA has two search processes: a global and a local search process. Poor coordination between these processes during population evolution can result in a slow or premature convergence. Global search expands the search area, reducing the risk of becoming trapped in local optima. Local search, on the other hand, accelerates convergence within a specific region of the solution space.

The performance of global and local searches is influenced by the value of *A*, which changes with the convergence factor *a*. Thus, the value of *a* is crucial for balancing these search capabilities.

The convergence factor *a* decreases linearly from 2 to 0 as the number of iterations increases. However, the WOA exhibits nonlinear changes during the optimisation process, so a linear change in the convergence factor cannot accurately reflect the algorithm's optimisation process. To balance the global and local search capabilities of the algorithm, an improved convergence factor scheme is proposed as follows:

$$a=\begin{cases} 2-e\left(\dfrac{t-1}{t_{\max}-1}\right)^2 & t\le 0.7t_{\max} \\ 4\dfrac{t_{\max}-t}{t_{\max}-1}-1 & 0.7t_{\max}<t\le t_{\max} \end{cases}. \tag{29}$$

The improved convergence factor *a* slows in early iterations, maintaining a relatively large *A* to enhance global search efficiency. In later iterations, it converges quickly, allowing *A* to remain small, thus increasing local search efficiency. This improved scheme effectively balances the global and local search performance of the algorithm.

5.4 Optimisation of motor regenerative braking force using improved WOA

The power of the electric mechanism is limited as follows:

$$0<F_e<F_{em}, \tag{30}$$

where *Fem* is the maximum braking force of the motor.

The feedback power formula of the axle motor is given by

$$P(F_e)=F_e v\eta-\left(\frac{F_e v\eta}{U}\right)^2 R, \tag{31}$$

where η is the product of the axle motor efficiency, the energy storage system charging feedback efficiency, and the transmission efficiency, U is the battery voltage, and R is the internal resistance of the battery.

The objective function G is set based on the motor's feedback power, which is then optimised using the WOA. The objective function G is written as

$$G = \frac{1}{P_{(Fe)}}. \tag{32}$$

To optimise the regenerative braking motor braking force, the population size is set to 100 and the number of iterations is set to 50.

6. Simulation results

To verify the effectiveness of the proposed EMB control strategy and the regenerative braking control strategy based on EMBs, models for both the EMB system and the regenerative braking control strategy were developed using MATLAB/Simulink. The overall vehicle model, including the battery and the motor, was constructed using AVL Cruise. The Simulink model was compiled into a DLL file for co-simulation with Cruise. The EMB control system model is depicted in Fig. 7, the regenerative braking control strategy model in Fig. 8, and the vehicle model in Fig. 9.

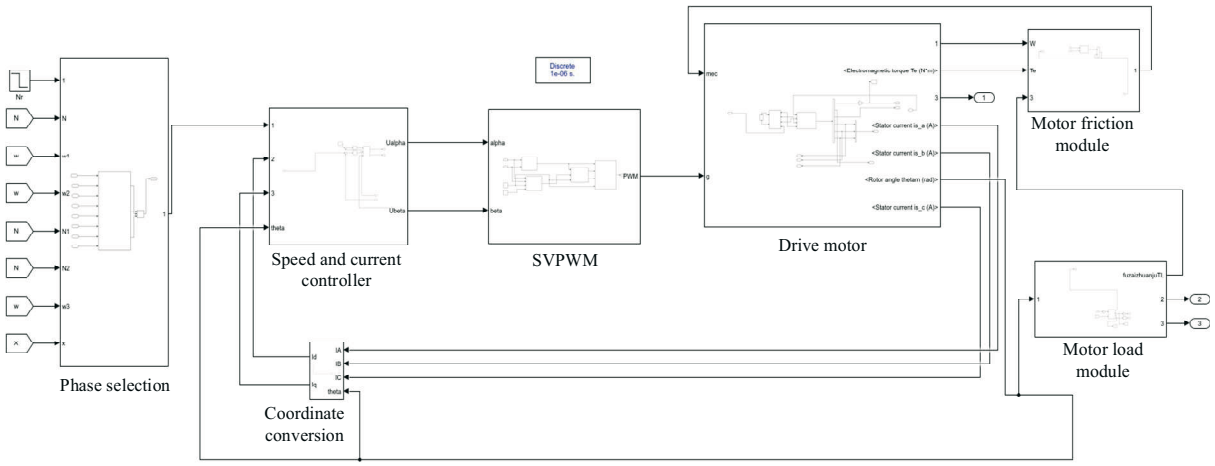

Fig. 7 Simulink model of EMB

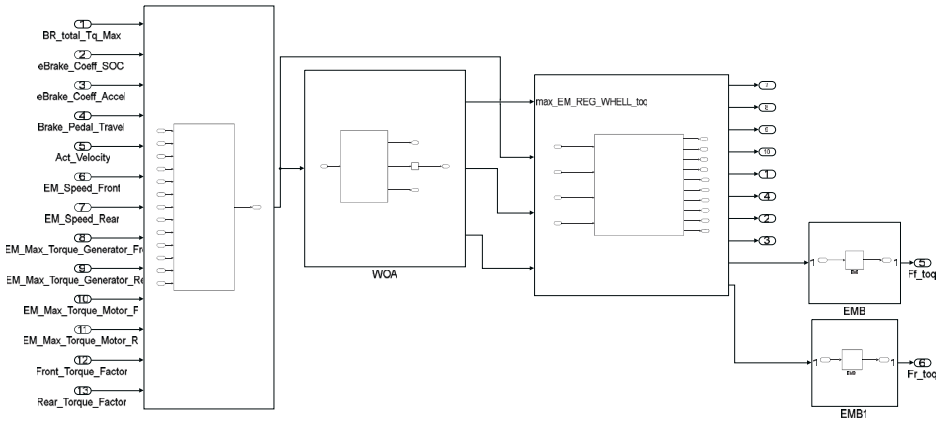

Fig. 8 Model of regenerative braking control strategy

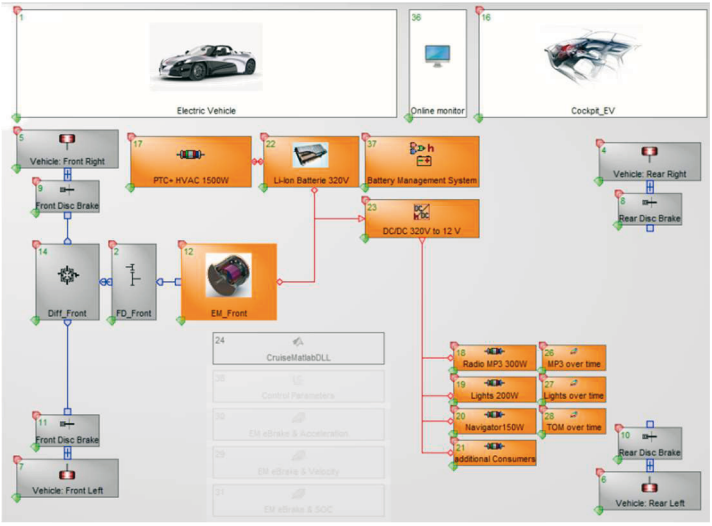

Fig. 9 Complete vehicle model in Cruise

6.1 EMB response

To assess the speed and accuracy of the EMBs, a 5 kN step brake force signal was applied to electric vehicles equipped with EMBs or EHBs. As shown in Fig. 10, the simulation results indicate that the braking gap for the EMBs is eliminated in only 0.04 seconds, compared to 0.23 seconds for the EHBs. This demonstrates an 82.61% improvement in gap elimination time. Additionally, the EMB system error is significantly smaller than the EHB's during the brake force tracking phase.

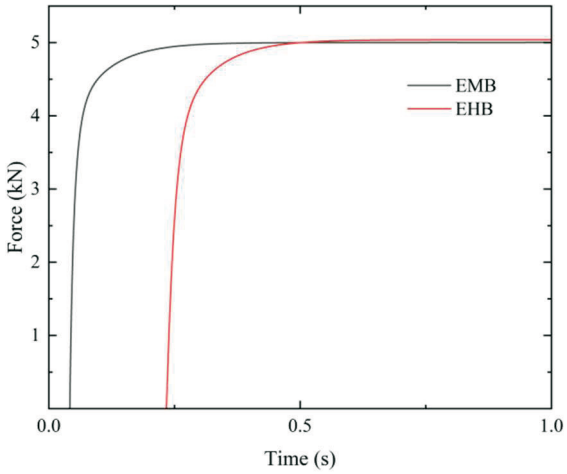

Fig. 10 Clamping force responses of EMBs and EHBs

Considering the brake gap, a 5 kN step signal is applied to the EMBs to verify the phased closed-loop control strategy designed in this paper. The ADRC parameters are listed in Table 1. The simulation results are shown in Fig. 11.

Table 1 ADRC parameters

Parameters	Values
β_{01}	1.83
β_{02}	1.76
β_2	2.28

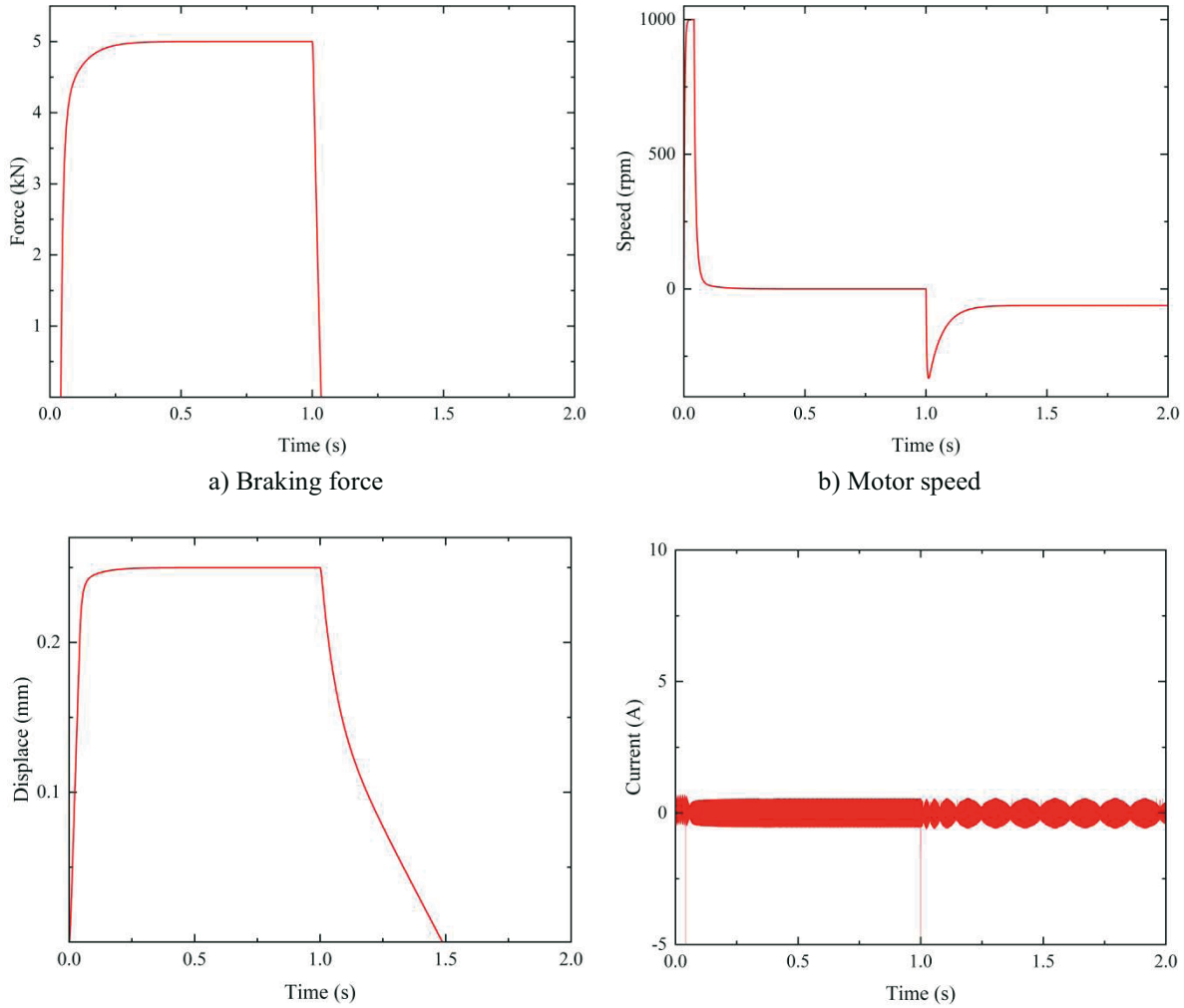

a) Braking force
b) Motor speed
c) Ball screw displacement
d) Motor current

Fig. 11 Response of the EMB system to a 5 kN braking force input

When the EMB controller receives the braking signal, the speed of the drive motor increases rapidly, reaching a maximum of 1,000 rpm in 0.02 seconds. The motor speed is shown in Fig. 11b. After the braking gap is eliminated, the system transitions to the braking force tracking phase, during which the speed quickly decreases. At 0.3 seconds, the braking force reaches the target value and the motor current stabilises, as shown in Fig. 11d.

At 1.0 second, a release brake signal is applied, initiating the brake gap regeneration phase. The brake force rapidly decreases to zero. Due to internal friction within the motor, the ball screw cannot return to its initial position. Therefore, a controlled reverse motion of the motor is required to form a fixed gap of 0.2 mm after the brake is released, so as to avoid wear of the brake pads. The simulation results are shown in Fig.11c.

6.2 Simulation results for the improved WOA

As shown in Fig. 12, the simulation results indicate that the improved WOA converges at the 18th iteration. This outperforms conventional algorithms, as it completes the optimisation two iterations earlier. This corresponds to a 10% reduction in the number of convergence generations and a 4.43% improvement in the fitness value of the optimal solution.

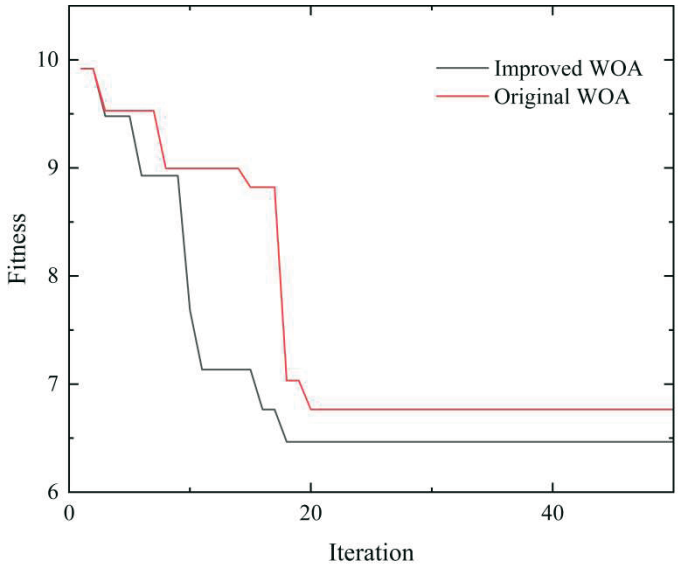

Fig. 12 Fitness evolution of different WOAs

6.3 Simulation results for the WLTC

The WLTC is a 23.25-kilometer test route developed by the United Nations Economic Commission for Europe and the International Automotive Working Group. It accurately simulates global driving conditions and is divided into four segments: low, medium, high, and ultra-high speed. The maximum speeds in each segment are 56.5 km/h, 76.6 km/h, 97.4 km/h, and 131.3 km/h, respectively. These speeds cover different types of driving scenarios and behaviours.

Fig. 13a shows changes in the vehicle speed, and Fig. 13b shows changes in the speed error under WLTC conditions. The proposed control strategy keeps the speed error below 1 km/h. Fig. 13c shows the state of charge (SOC) of the battery, which begins at 60%. At the end of the cycle, the vehicle with EHBs retains a charge of 44.5%. Meanwhile, the vehicle with EMBs and the original WOA retains a charge of 45.5%, while the vehicle with EMBs and the improved WOA retains a charge of 46.2%. These results indicate that the optimised control strategy effectively conserves battery power. Fig. 13d shows the motor's peak torque during regenerative braking for the three control strategies: 139.4 Nm for EHBs, 215.21 Nm for the original WOA, and 238.42 Nm for the improved WOA. Table 2 shows that the vehicle with EMBs and the improved WOA saves 1.7% of the charged energy compared to the vehicle with EHBs and 0.7% compared to the vehicle with the original WOA. Further data analysis shows that for the vehicles equipped with EMBs and a 40 kWh battery, the energy recovery is 2,448 kJ higher than that of the vehicles equipped with EHBs and 1,008 kJ higher than that of the vehicles with the original WOA. Also, the regenerative braking motor torque increases by 41.53% and 9.74% against the two benchmarks, respectively. This confirms the effectiveness of the proposed control strategy.

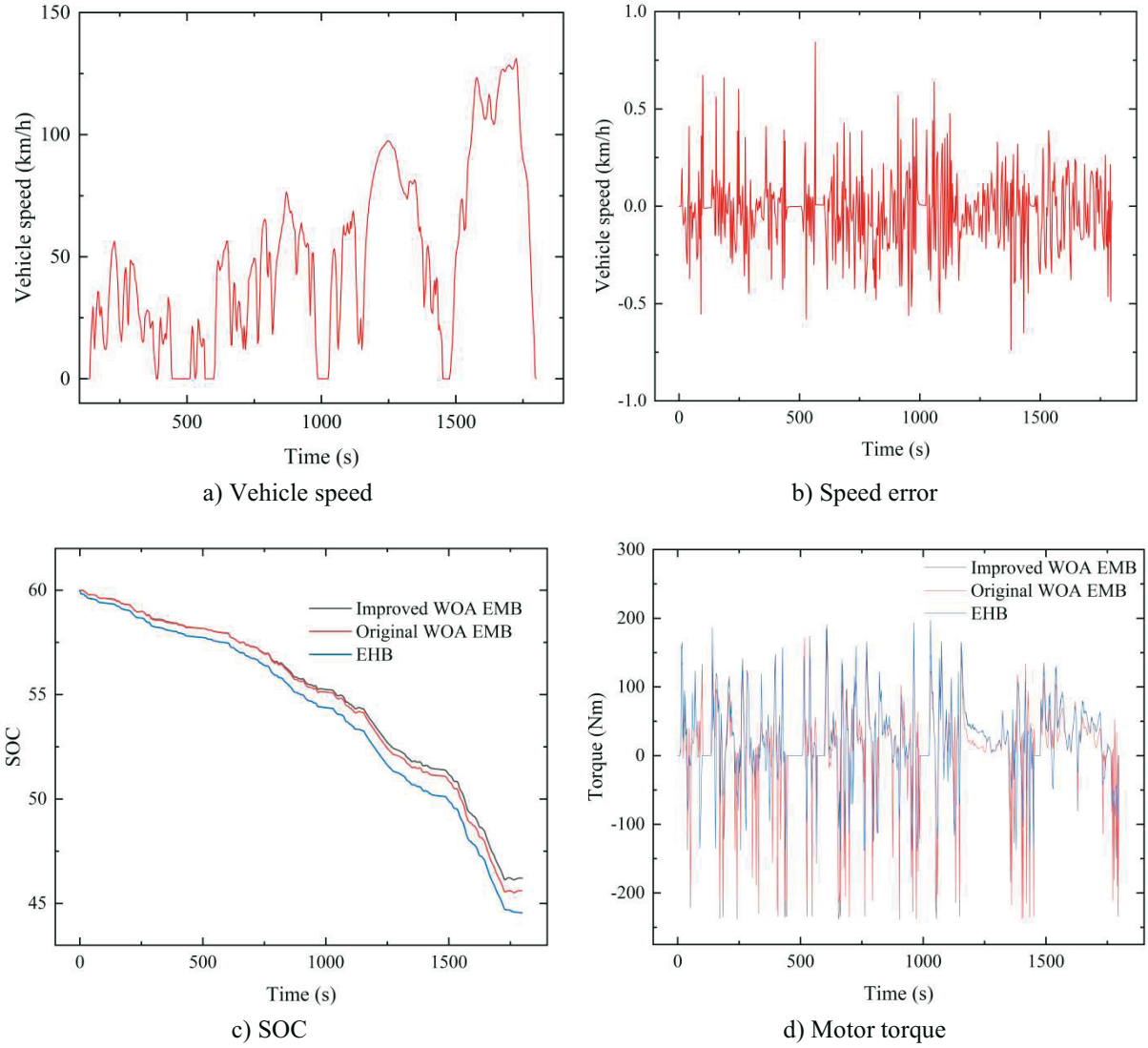

a) Vehicle speed b) Speed error

c) SOC d) Motor torque

Fig. 13 Simulation results for WLTC

Table 2 Comparison of simulation results for WLTC

Parameters	EHB	EMB/Original WOA	EMB/Improved WOA
SOC%	60-44.5	60-45.5	60-46.2
Maximum torque of motor /Nm	139.4	215.21	238.42

6.4 Simulation results for CLTC

The CLTC is a 14.48-kilometer test route developed by the China Automotive Technology Research Centre and other organisations. It aligns more closely with Chinese road regulations and driving habits. Compared to other test cycles, the CLTC more accurately reflects the country's actual driving conditions.

Fig. 14a and Fig. 14b show changes in the vehicle speed and the speed error under CLTC conditions. The proposed control strategy maintains a speed error of less than 1 km/h. Figure 14c shows the SOC of the battery, which starts at 60%. At the end of the cycle, the vehicle equipped with EHBs has a remaining charge of 50.4%. Meanwhile, the vehicle with EMBs and the original WOA has 51%, and the vehicle with EMBs and the improved WOA has 51.5% of charge. These results further support the conclusion that the optimised control strategy saves battery power. Figure 14d shows the motor's peak torque during regenerative braking for the

three strategies: 150.8 Nm for EHBs, 215.44 Nm for the original WOA, and 238.65 Nm for the improved WOA. Table 3 shows that the vehicle with EMBs and the improved WOA saves 1.1% of the charged energy compared to the vehicle with EHBs and 0.5% compared to the vehicle with the original WOA. Further data analysis shows that for the vehicles equipped with EMBs and a 40 kWh battery, the energy recovery is 1,584 kJ higher than that of the vehicles equipped with EHBs and 720 kJ higher than that of the vehicles with the original WOA. Also, the regenerative braking motor torque increases by 36.81% and 9.73% against the two benchmarks, respectively. This further validates the effectiveness of the proposed control strategy.

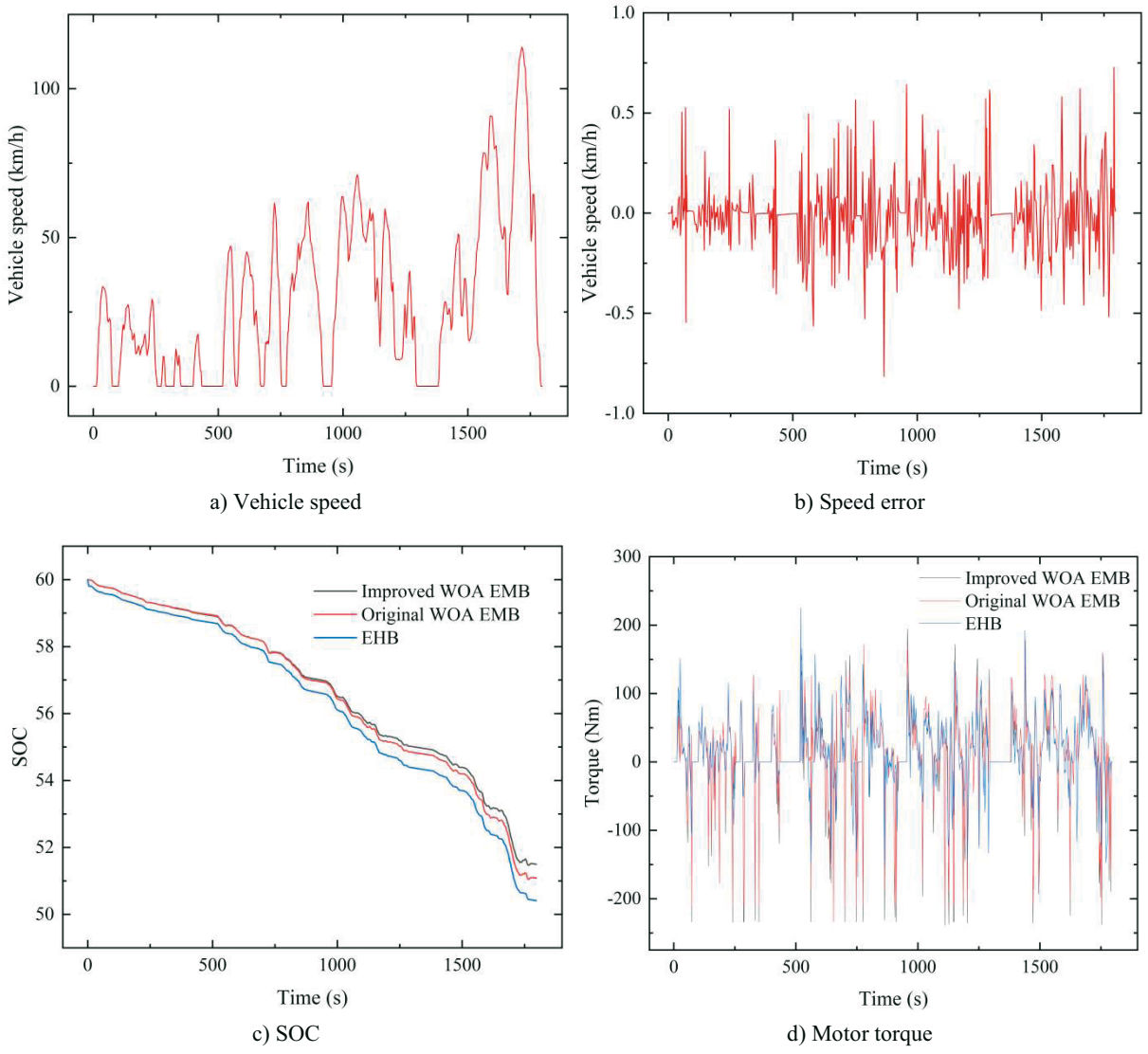

Fig. 14 Simulation results for WLTC

Table 3 Comparison of simulation results for CLTC

Parameters	EHB	EMB/Original WOA	EMB/Improved WOA
SOC%	60-50.4	60-51	60-51.5
Maximum torque of motor /Nm	150.8	215.44	238.65

7. Conclusions

This paper presents a brake energy recovery control strategy based on EMBs, utilizing an improved WOA to optimise the parameters of the ADRC and the motor braking force during regenerative braking. The simulations were conducted using two typical driving cycles: WLTC and CLTC.

The proposed three-stage control strategy for the EMB system can control the rotation of the drive motor to quickly eliminate the braking gap during the initial phase. In the braking force tracking phase, the ADRC algorithm is more accurate and faster than conventional EHB configurations in following the target braking force. It also outperforms EHBs in terms of eliminating the braking gap time and the steady-state error. During the brake gap generation phase, the system can reverse the motor to establish a fixed gap. This prevents wear on the brake disc and pads. This feature makes the EMB system faster and more accurate, which helps extend the life of the brakes and keep you safer on the road.

The ideal brake force distribution curve and the ECE regulation line are used to create a brake force distribution strategy based on safety zone rules. This strategy makes sure that the force applied when braking is evenly distributed between the front and the rear axles. The motor braking force is enhanced using the improved WOA. This makes the torque and the current during regenerative braking go up. This also improves the energy recovery efficiency and results in a longer driving range of electric vehicles.

In actual vehicles, sensor noise, actuator dynamic response delays, and sudden changes in the tire–road friction coefficient can actually greatly affect control accuracy. To address these uncertainties, the three-stage control strategy based on ADRC inherently possesses certain disturbance rejection capabilities, as the core idea of ADRC is to estimate and compensate for the "total disturbance" of the system (including both internal and external uncertainties).

To further enhance the system's robustness, our future research activities will deal with explicitly accounting for parametric uncertainties and disturbances in the optimisation objective, thereby designing a more robust cost function, introducing an adaptive strategy that uses road condition recognition to adjust the rules for distributing braking force in real time, and conducting hardware-in-the-loop (HIL) testing to validate the algorithm's performance in environments that more closely resemble real-world conditions.

REFERENCES

[1] Zhang, H.; Xue, B.; Wang, L.; Chen, L.; Huang, K.; Chang, Z.; Yu, Y. The electric vehicles recycling process to carbon neutrality mission in China tends to be negative: Depending on the technology transition. *Polish Journal of Environmental Studies* **2023**, 32 (2), 1941-1948. https://doi.org/10.15244/pjoes/157219

[2] Tang, Y.; Zhang, Q.; Liu, B.; Li, Y.; Ni, R.; Wang, Y. What influences residents' intention to participate in the electric vehicle battery recycling evidence from China. *Energy* **2023**, 276, 127563. https://doi.org/10.1016/j.energy.2023.127563

[3] Li, C.; Zhuo, G.; Tang, C.; Xiong, L.; Tian, W.; Qiao, L.; Cheng, Y.; Duan, Y. A review of electro-mechanical brake (EMB) system: structure, control and application. *Sustainability* **2023**, 15 (5), 4514. https://doi.org/10.3390/su15054514

[4] Ahn, J. K.; Jung, K. H.; Kim, D. H.; Jin, H. B.; Kim, H. S.; Hwang, S. H. Analysis of a regenerative braking system for Hybrid Electric Vehicles using an Electro-Mechanical Brake. *International Journal of Automotive Technology* **2009**, 10 (2), 229-234. https://doi.org/10.1007/s12239-009-0027-z

[5] Schrade, S.; Nowak, X.; Verhagen, A.; Schramm, D. Short review of EMB systems related to safety concepts. *Actuators* **2022**, 11 (8), 214. https://doi.org/10.3390/act11080214

[6] Park, G.; Choi, S.; Hyun, D. Development of clamping force estimation algorithm and clamp-force sensor calibration on electromechanical brake systems. *Transactions of the Korean Society of Automotive Engineers* **2016**, 24 (3), 365-371. https://doi.org/10.7467/KSAE.2016.24.3.365

[7] Fu, Y. F.; Hu, X.; Wang, W.; Ge, Z. Simulation and experimental study of a new electromechanical brake with automatic wear adjustment function. *International Journal of Automotive Technology* **2020**, 21 (1), 227-238. https://doi.org/10.1007/s12239-020-0022-y

[8] Ki, Y. H.; Lee, K. J.; Cheon, J. S.; Ahn, H. S. Design and implementation of a new clamping force estimator in electro-mechanical brake system. *International Journal of Automotive Technology* **2013**, 14 (5), 739-745. https://doi.org/10.1007/s12239-013-0081-4

[9] Li, Y.; Shim, T.; Shin, D. H.; Lee. S.; Jin, S. Control system design for electromechanical brake system using novel clamping force model and estimator. *IEEE Transactions on Vehicular Technology* **2021**, 70 (9), 8653-8668. https://doi.org/10.1109/TVT.2021.3095900

[10] Line, C.; Manzie, C.; Good, M. C. Electromechanical brake modeling and control: From PI to MPC. *IEEE Transactions on Control Systems Technology* **2008**, 16 (3), 446-457. https://doi.org/10.1109/TCST.2007.908200

[11] Wei, Z.; Xu, J.; Halim, D. Clamping force control of sensor-less electro-mechanical brake actuator. *2017 IEEE International Conference on Mechatronics and Automation (ICMA)* **2017**, 764-769. https://doi.org/10.1109/ICMA.2017.8015912

[12] Lee, C.F.; Manzie, C. Active brake judder attenuation using an electromechanical brake-by-wire system. *IEEE/ASME transactions on mechatronics* **2016**, 21 (6), 2964-2976. https://doi.org/10.1109/TMECH.2016.2571318

[13] Zhao, F.; Liu, X.; Zhang, H. Automobile industry under China's carbon peaking and carbon neutrality goals: Challenges, opportunities, and coping strategies. *Journal of Advanced Transportation* **2022**, 1-13. https://doi.org/10.1155/2022/5834707

[14] Nourbakhsh, Borujerd. S. V.; Soleimani, A. Fuzzy logic approach for failure analysis of li-ion battery pack in electric vehicles. *Engineering Failure Analysis* **2023**, 149, 107233. https://doi.org/10.1016/j.engfailanal.2023.107233

[15] Che, C.; Wang, Y. W.; Lu, Q. W. An effective utilization scheme for regenerative braking energy based on power regulation with a genetic algorithm. *IET Power Electronics* **2022**, 15 (13), 1392-1408. https://doi.org/10.1049/pel2.12312

[16] Li, X.; Zhang, X.; Wang, Y. Regenerative braking control strategies with fixed ratio and variable ratio braking forces optimization distribution for electric vehicles during downhill process. *International Journal of Automotive Technology* **2022**, 23 (3), 667-681. https://doi.org/https://doi.org/10.1007/s12239-022-0061-7

[17] Zheng, Z.; Liang, C.; Lv, H. Research on composite braking mode switching strategy based on fuzzy algorithm. advanced theory and simulations. *Advanced Theory and Simulations* **2023**, 6 (2), 2200789. https://doi.org/10.1002/adts.202200789

[18] Zhang, Q.; Yuan, Y. A novel coordinated control strategy of regenerative braking and anti-lock system for electric vehicles. *Proceedings of the Institution of Mechanical Engineers Part D: Journal of Automobile Engineering* **2024**, 238 (2-3), 304-319. https://doi.org/10.1177/09544070221130416

[19] Mei, P.; Karimi, H. R.; Yang, S.; Xu, B.; Huang, C. An adaptive fuzzy sliding-mode control for regenerative braking system of electric vehicles. *International Journal of Adaptive Control and Signal Processing* **2022**, 36 (2), 391-410. https://doi.org/10.1002/acs.3347

[20] Yang, K.; Chen, L.; Chen, Y.; Ma, C.; Tan, D.; Wang, W. Structure design and advantage research for bidirectional synchronous force-increasing EMB actuator. *Engineering Research Express* **2024** 6 (1), 015051. https://doi.org/10.1088/2631-8695/ad1ea2

[21] Chen, L.; Sun, X. D.; Jiang, H. B.; Xu, X. High Performance control of a permanent magnet synchronous motor for electric vehicle applications. *Journal of Computational and Theoretical Nanoscience* **2014**, 11 (3), 706-710. https://doi.org/10.1166/jctn.2014.3415

[22] Wang, C.; Peng, J. D.; Pan, J. F. A Novel friction compensation method based on stribeck model with fuzzy filter for PMSM servo systems. *IEEE Transactions on Industrial Electronics* **2023** 70 (12), 12124-12133. https://doi.org/10.1109/TIE.2022.3232667

[23] Li, J.; Wang, M. C.; He, R.; Zhang, J. A design of electromechanical brake system triple-loop controllers using frequency domain method based on Bode plote. *2011 International Conference on Transportation, Mechanical, and Electrical Engineering (TMEE)* **2011**, 795-798. https://doi.org/10.1109/TMEE.2011.6199322

[24] Yang, H.; Li, Z.; Wang, J.; Tao, L.; Zhou, L. Modeling for clamping force and hierarchical PI control with ADRC for EMB system. *2023 26th International Conference on Electrical Machines and Systems (ICEMS)* **2023**, 1938-1943. https://doi.org/10.1109/ICEMS59686.2023.10345016

[25] Zhou, S. W.; Liu, J. S.; Wang, Z. L.; Sun, S. H. Research on design optimization and simulation of regenerative braking control strategy for pure electric vehicle based on EMB systems. *Transactions of Famena* **2023**, 47 (4), 33-49. https://doi.org/10.21278/TOF.461019420

[26] Zhao, J.; Chen, Z.; Zhu, B. Precise active brake-pressure control for a novel electro booster brake system. *IEEE Transactions on Industrial Electronics* **2019**, 67 (6), 4774- 4784. https://doi.org/10.1109/TIE.2019.2924613

[27] Zhou, S. Wang, Q.; Liu, J. Control strategy and simulation of the regenerative braking of an electric vehicle based on an electromechanical brake. *Transactions of Famena* **2022**, 46 (1), 23-40. https://doi.org/10.21278/TOF.474045522

[28] Nadimi-Shahraki, M. H.; Zamani, H.; Varzaneh, Z.; Mirjalili, S. A systematic review of the whale optimization algorithm: theoretical foundation, improvements, and hybridizations. *Archives of Computational Methods in Engineering* **2023**, 30 (7), 4113-4159. https://doi.org/10.1007/s11831-023-09928-7

[29] Mirjalili S. Handbook of Whale Optimization Algorithm: Variants, Hybrids, Improvements, and Applications. Academic Press, 2024. https://doi.org/10.1016/C2021-0-02761-9

Submitted: 05.12.2024

Accepted: 03.11.2025

Zhen Lei
Hongming Lyu *
School of Automotive Engineering,
Yancheng Institute of Technology,
Yancheng, China
*Corresponding author:
Hongming_lv@ycit.edu.cn